REPORT DOCUMENTATION PAGE

AFRL-SR-AR-TR-04-

0343

1. AGENCY USE ONLY (Leave blank)	2. REPORT DATE	3. REPORT TYPE A
	15 May 2003	15-Nov-1999 to 31-Jan-2003

4. TITLE AND SUBTITLE
Three-dimensional structure of turbulent scalar fields with applications in aerooptics

5. FUNDING NUMBERS
F49620-00-1-0036

6. AUTHOR(S)
Paul E. Dimotakis
Christopher Martin

7. PERFORMING ORGANIZATION NAME(S) AND ADDRESS(ES)

California Institute of Technology
1200 E California Blvd.
Pasadena, CA 91125

8. PERFORMING ORGANIZATION REPORT NUMBER

9. SPONSORING / MONITORING AGENCY NAME(S) AND ADDRESS(ES)

AFOSR
4015 Wilson Blvd., Room 713
Arlington, VA 22203-1954

NA

10. SPONSORING / MONITORING AGENCY REPORT NUMBER

11. SUPPLEMENTARY NOTES

20040709 020

12a. DISTRIBUTION / AVAILABILITY STATEMENT
Approved for public release; distribution is unlimited

12b. DISTRIBUTION CODE

13. ABSTRACT ***(Maximum 200 Words)***

This is the final report for AFOSR Grant F49620-00-1-0036, which ended 31 Jan 2003. This program aimed to develop an interferometric technique for mitigating the effects of turbulence on visible-light imaging, complementary to techniques such as Adaptive Optics (AO) or speckle imaging. This technique employs a rotation shearing interferometer and high-speed, low-noise digital imaging system. Where an AO system would employ a complex high-bandwidth electro-mechanical system to mitigate the effects of turbulence, this interferometric technique relies on a novel (low-cost) optical design, high-speed detector electronics, and digital post-processing to obtain images. One significant advantage of this technique is the use of a large-format detector, which enables correction of aberrating fields with power at far higher wavenumbers than AO systems can accommodate. This technique has undergone a number of successful laboratory tests under weakly aberrating conditions, and data obtained at an astronomical observatory, currently under analysis, has passed several operational tests.

14. SUBJECT TERMS

15. NUMBER OF PAGES
16

16. PRICE CODE

17. SECURITY CLASSIFICATION OF REPORT	18. SECURITY CLASSIFICATION OF THIS PAGE	19. SECURITY CLASSIFICATION OF ABSTRACT	20. LIMITATION OF ABSTRACT
Unclassified	Unclassified	Unclassified	UL

6/4/03

GRADUATE AERONAUTICAL LABORATORIES
CALIFORNIA INSTITUTE of TECHNOLOGY
Pasadena, California 91125

Three-dimensional structure of turbulent scalar fields with applications in aerooptics

Paul E. Dimotakis* and Christopher Martin**

Air Force Office of Scientific Research
Grant No. F49620-00-1-0036

Final Scientific Report
15 November 1999 through 31 January 2003

15 May 2003

* John K. Northrop Professor of Aeronautics and Professor of Applied Physics
** Professor of Physics

Summary

This research effort comprised the development and testing of a novel interferometric technique for imaging through turbulence, coupled with the development of a high-speed, low-noise imaging system for maximum efficiency, as required for imaging through turbulence. There were two primary thrusts to this effort:

- Development and testing of the Quadrature Phase Interferometer (QPI)
- Development and testing of high-speed, low-noise digital imaging systems

In laboratory tests and at an astronomical observatory, the QPI has shown that it can mitigate the effects of turbulence on optical image formation. The laboratory tests, obtained under conditions of weak turbulence, show excellent imaging performance and demonstrate the potential of near-diffraction-limited imaging. Further improvements in the design and operation of the interferometer are underway, as is analysis of data recorded at the Hale 200″ Telescope at Palomar Observatory.

Development and testing of the Kilo-Frame per Second (KFS) high-speed, low-noise CCD camera has provided the best noise performance at high frame rates over a large format (1024 × 1024 pixel) camera to date, measuring under 26 e^-/pixel rms noise for a 5 ms full-frame, unbinned readout and 15.5 e^-/pixel for a 10 ms, full-frame, 2×2 binned readout time. The design and fabrication of a next-generation low-noise system, a Hybrid Imaging Technology (HIT)-KFS CCD, was begun during this period and is continuing at this time. The HIT technology should enable a further reduction in read noise by a factor of 2-3, for comparable read times.

Introduction

The development of the QPI technique complements alternative imaging programs with similar goals. The QPI is a rotation-shearing interferometer, which has some advantages over Adaptive Optics (AO), speckle interferometry, and non-redundant masking interferometry, under a number of observing conditions. The QPI has the potential to construct images in the presence of aberrating fields containing power at high spatial wavenumbers. The wavefront resolution of the QPI is up to 20 times that of contemporary AO systems. As presently implemented, QPI has 512 pixels spanning the input pupil, compared to ~ 30 actuators across the pupil in AO systems. The QPI is unaffected, to first order, by wavefront scintillation, which arises under conditions of strong turbulence, or long propagation distances through turbulence, or when observing at short wavelengths. Such scintillation, if uncorrected, degrades imaging performance, even if phase aberrations across the wavefront are removed. The external calibration requirements of QPI are less stringent than that of other passive image reconstruction techniques (e.g., speckle interferometry).

The principles behind the QPI technique are described in detail in Kern *et al.* (2001). The QPI is a 180-degree rotation shearing pupil-plane interferometer, in a Mach-Zender arrangement. The instrument interferes two copies of the input pupil, rotated by 180 degrees with respect to one another. This is shown schematically in Fig. 1. The Mach-Zender arrangement allows for complementary interferograms to be recorded

simultaneously, each of which shows the interference between the same two copies of the input pupil, but with 180° of interferometric phase difference between corresponding points in the two interferograms. Where one interferogram is bright, the other is dark.

The choice of a 180-degree rotation shear introduces a redundancy in the information content of the interferograms, which is exploited by introducing an instrumental phase shift in half of each interferogram. For each point in the interferograms, this instrumental phase offset allows four measurements to be made simultaneously (see Fig. 1 for examples), with four different instrumental phase (path length difference) contributions. This simultaneous measurement of four intensities allows for an instantaneous determination of the full complex visibility, as well as a map of the wavefront amplitude across the pupil. The complex visibility is the fundamental measurement made by the interferometer. It is convenient to discuss the modulus and phase of the complex visibility separately, as $\gamma(u,v) = V(u,v) \exp\{i\, \phi(u,v)\}$, where u and v denote the location in the interferograms (equivalent to angular wavenumbers). The Fourier Transform of the complex visibility is the reconstructed image. Phase aberrations in the input wavefront affect the measured visibility phase, $\phi(u,v)$, but not the measured visibility modulus, $V(u,v)$. The phase aberrations can be eliminated from the complex visibility by an averaging technique (circular averaging of the phase gradients).

Interferograms measured by the QPI have intensities modulated by turbulent aberrations, which may have characteristic timescales of tens of milliseconds, or less. For timescales

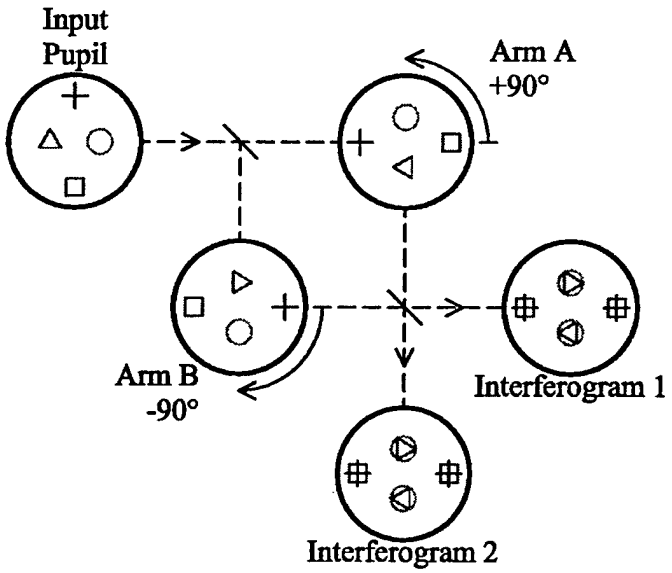

Fig. 1. Schematic representation of rotation-shearing interferometer operation. Four points in the input pupil are shown, which pass through a beamsplitter into the two arms of the interferometer, then through a second beamsplitter to recombine into two interferograms. The superposition of points from opposite sides of the input pupil causes the intensity in the interferograms to be modulated by the visibility function of the object under study. Each interference pair (e.g., cross and square, or circle and triangle) appears in two places in each of the two output interferograms, allowing four measurements for each interference pair.

this short, the important performance issues are signal-to-noise ratio of the measurements and exposure duty cycle. Low detector noise emerges as an important attribute because short exposures do not permit the collection of large amounts of light. Short readout times are desirable both to maximize the net exposure in a given period of time, and to permit the formation of a contiguous time-series of observations to track turbulent aberrations.

The KFS digital-imaging system uses a custom-built (1024×1024)-pixel CCD, optimized to deliver low read noise (under 30 e^-/pixel rms) for full-frame read times as short as 5 ms. It was developed as part of this effort, and under DURIP Grant F49620–95–1–0199, and AFOSR Grants F49620–98–1–0052 and F49620–01–1–0006 and provides the best solution for the imaging demands of the QPI. It is described in detail in Kern *et al.* (2001).

QPI Experimental Progress: Year 1

QPI laboratory testing in the first year of effort focused on simple imaging experiments. The object imaged in these experiments was a pinhole, with a diameter slightly larger than the diffraction-limited resolution of the interferometer. The QPI measures the object's complex visibility function, which for a uniformly illuminated disc is an Airy function. The first zero of the Airy function occurs at an angular wavenumber given by $1.2/d$, where d is the angular diameter of the pinhole. In addition to verifying the basic performance of the interferometer, this observation showed that the peak visibility modulus observed by this system was effectively unity. The peak visibility modulus can be reduced by a number of conditions, but this experiment showed that the QPI does not suffer from instrumental visibility degradation. These observations are described in more detail in Kern *et al.* (2001). A plot of the squared visibility modulus versus angular

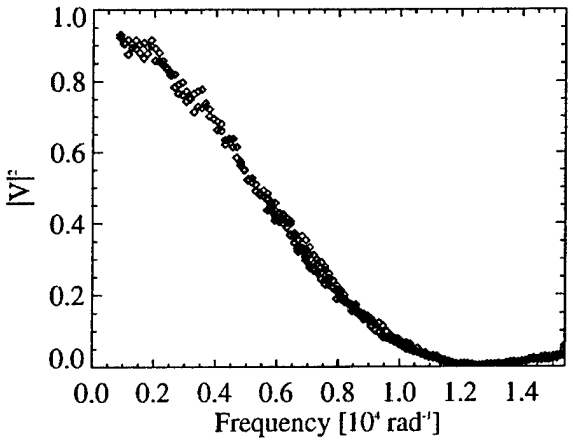

Fig. 2. Visibility plot for pinhole. This is a plot of the radial dependence of the square of the measured visibility modulus on position in the interferogram. Position in an interferogram is equivalent to angular wavenumber (labeled frequency in this plot) in the complex visibility function. The object under study is a pinhole, with angular diameter 0.1 milliradian (linear diameter 25 μm). This plot is not corrected or calibrated in any way, so the high visibility near zero wavenumber indicates that the instrument does not degrade the visibility modulus.

wavenumber, measured for this pinhole, is shown in Fig. 2.

QPI Experimental Progress: Year 2

A full imaging demonstration was performed in the second year of effort. A complex object was illuminated and image reconstructions were performed in both the absence and presence of turbulence in the propagation path. Aberrations were implemented by a turbulent helium jet introduced in the propagation path and were increased in strength until the object became unrecognizable in a direct image.

The interferometric image-reconstruction algorithm used for this experiment involves several steps. The controlled laboratory setting allows for careful calibration of the interferometer. Maps of the system throughput were obtained for the arms of the interferometer, the A and B arms, independently. Throughput variations, caused principally by dust on optics at various point in the propagation path, can be completely removed by this calibration. Subsequent exposures taken through the interferometer are then normalized by the throughput maps.

Each normalized exposure contains two interferograms, numbered 1 and 2. The first step in calculating the complex visibility for an exposure is to calculate a renormalized difference of Interferograms 1 and 2. The intensity of a given point in Interferogram 1 depends on the wavefront amplitude, visibility modulus, and visibility phase. The intensity of the corresponding point in Interferogram 2 has the same contribution from

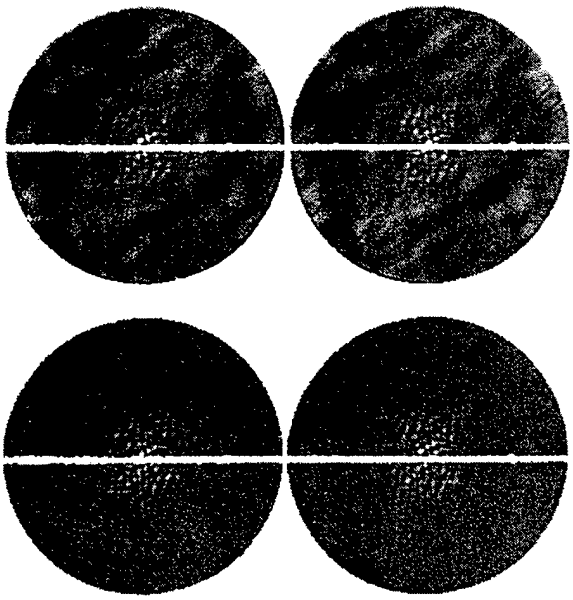

Fig. 3. Normalized interferograms, and renormalized differences. The top two panels are normalized Interferograms 1 and 2 from an exposure, the bottom panels are the difference divided by the sum of the two interferograms. The two bottom panels are exact negatives of one another; only one of the bottom two panels is needed. The wavefront amplitude fluctuations visible in the top panels are absent from the bottom panels. The blank band through the middle of each interferogram is due to the split between the mirrors forming the upper and lower halves.

wavefront amplitude and visibility modulus, but differs in phase by 180°. Each point in the renormalized difference is the difference of corresponding points in the two interferograms, divided by the sum. The renormalized difference has no dependence on the wavefront amplitude, only on visibility modulus and phase. Without using both interferograms, visibility measurements would be corrupted by the wavefront amplitude variations. An example pair of interferograms, before and after subtraction, is shown in Fig. 3. The most striking difference between the normalized interferograms and renormalized differences in Fig. 3 is the absence of amplitude fluctuations in the renormalized difference. These amplitude fluctuations are not static throughput variations, but rather turbulent fluctuations (scintillation), to which the renormalized difference is insensitive, to first order.

The renormalized difference is further divided into upper and lower halves, composing the quadrants needed to establish quadrature phase relationships. The instrumental phase offset, which would ideally equal 90° (or $\lambda/4$), as described in Kern *et al.* (2001), in practice must be treated as an independent variable for every point. This changes Eqs. 9 and 10 from the form described in Kern *et al.* (2001), to

$$V(\vec{u}) = \sqrt{\delta_U^2(\vec{x}) + [\delta_U(\vec{x})/\tan\theta(\vec{x}) + \delta_L(\vec{x})/\sin\theta(\vec{x})]^2}\,/\,[\sigma_U(\vec{x}) + \sigma_L(\vec{x})],$$

$$\phi(\vec{u}) = \tan^{-1}\{[\delta_U(\vec{x})\cos\theta(\vec{x}) + \delta_L(\vec{x})]/[\delta_U(\vec{x})\sin\theta(\vec{x})]\},$$

where θ is the instrumental phase offset. These equations reduce to Eqs. 9 and 10 in Kern *et al.* (2001) when $\theta = 90°$. Because these equations compare points in the upper half of the renormalized difference to corresponding (diametrically opposed) points in the lower half, it is sufficient to refer to positions only in the upper half of the renormalized difference, also known as the upper quadrant.

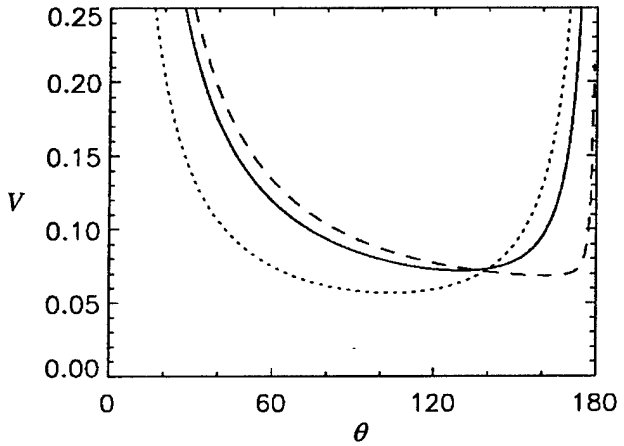

Fig. 4. Determination of θ for a single point, using the object shifting method. The three plots represent calculated values of V for a single point, in each of three calibration exposures. The calibration exposures were taken with small shifts of the object, causing the visibility phase to vary, but leaving the visibility modulus the same in all exposures. Values of V are calculated for all possible values of θ, but only one value of θ gives the same (correct) value of V for all three calibration exposures. This technique applied to the point shown above gives a very small uncertainty in θ, while for most points the uncertainty is on the order of 10-20°.

For this experiment, θ is determined using a set of calibration exposures. These differ from one another by the introduction of small lateral shifts in the object plane position. A shift in the object plane position introduces a constant phase gradient in the complex visibility, but leaves the visibility modulus unchanged everywhere. While the true visibility modulus is unchanged in the calibration exposures, the measured visibility modulus, V, at a given point will have the same value in all calibration exposures only if the correct value of θ is used. This technique allows an independent determination of θ for each pixel in the upper quadrant. A sample set of plots, to determine θ for a single point in the upper quadrant, is shown in Fig. 4.

The QPI obtains direct images simultaneously with the interferograms, allowing a comparison of the performance of the interferometric image reconstruction with that of a direct image, through identical turbulent conditions. In this experiment, the unaberrated direct images and interferometric images are of similar quality, as shown in Fig. 5. The aberrated direct images become unrecognizable, while the aberrated interferometric images are of nearly the same quality as the unaberrated interferometric images.

In this experiment, spatial wavenumbers of the aberrations were small, and the process of reconstructing images from the interferograms was straightforward, requiring only the simplest averaging system to remove the aberrations from the phase of the complex visibility. In each aberrated exposure, the best-fit constant phase gradient (equivalent to a

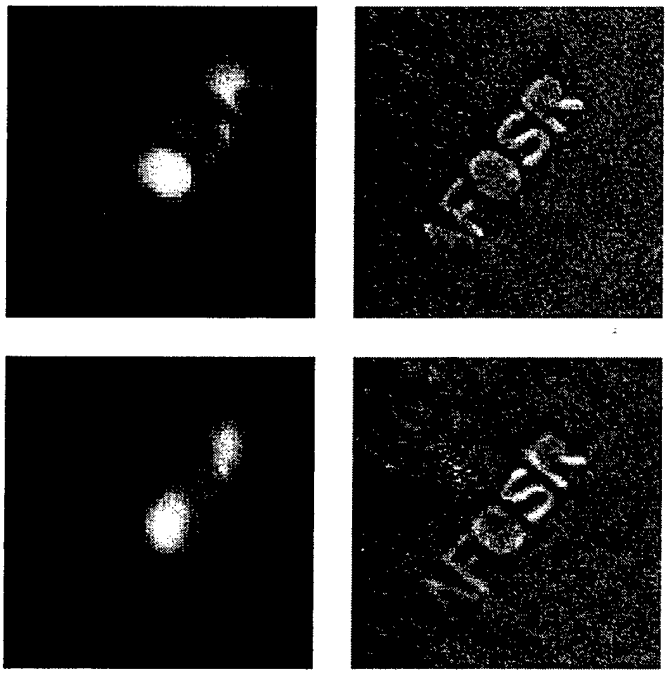

Fig. 5. Comparison of direct and interferometric imaging, without and with aberrations present. The left panels are direct images of a test object, the right panels are interferometric images. The upper panels have no external aberrations, the bottom panels were imaged through a turbulent helium jet. The upper images (both direct and interferometric) are simultaneous, and the lower images are simultaneous. The aberrated interferometric image is only slightly degraded, while the aberrated direct image is unrecognizable.

wavefront tilt) was subtracted from the visibility phase. The resulting complex visibility was Fourier transformed to obtain interferometric images. The aberrated images, both direct and interferometric, are formed as the average of 12 exposures. This experiment demonstrated the weak-turbulence performance of the interferometric imaging technique.

QPI Experimental Progress: Year 3

In the third year of effort, the QPI and KFS were taken to Palomar Observatory to be used with the Hale 200″ Telescope. The targets of these observations were chosen to demonstrate simple visibility measurements. These targets were bright, unresolved stars (pointlike objects), close binary stars, and "giant" stars. The visibility functions of these objects are simple, allowing a real-time determination of the gross performance of the system, by visual inspection of the interferograms. The challenge of these observations is to perform an interferometric correction over the full 200″ aperture of the telescope, which spans many atmospheric coherence lengths. Here, $D \sim 50\ r_0$, where r_0 is Fried's (1966) coherence length, $r_0 \sim 10$ cm. The analysis of this data is ongoing. Preliminary results show that the measured visibility modulus is consistent with expectations and that quadrature phase relationships exist between the interferograms. Visibility phase maps have not yet been constructed from these measurements.

The experiment at Palomar Observatory highlighted an important improvement necessary for reliable use of the QPI. Flexure in the telescope delivered an input pupil that moved with respect to the QPI as targets were acquired. Compensation for this flexure required realignments internal to the interferometer, which were not anticipated. These realignments were slow and imperfect, and resulted in a loss of observing time and inferior data. The simplest solution to this problem is the use of an additional mirror guiding the telescope light into the interferometer, arranged in such a way that motion of the input pupil, caused by flexure of the telescope, can be compensated by motion of a single mirror. The designs for this improvement have been completed, and will be implemented before a next visit to Palomar Observatory (not yet scheduled).

The QPI has various alignment requirements, each of which impact the data in different ways. The motion of the input pupil with respect to the QPI, mentioned above, results in an imperfect overlap of the pupil images that form interferograms. This is shown diagrammatically in Fig. 6. The QPI defines a center about which the two pupil images are rotated, through 90 degree angles, in opposite directions in arms A and B. When the pupil images are overlaid to form interferograms, there are regions of each pupil image that do not interfere with regions from the other pupil image. The impact of this misalignment is a loss of useful area in the interferograms, particularly at high angular frequencies (the outer regions of the interferograms). If this misalignment becomes large, the pupil images may not overlap at all, resulting in no interference. In general, in the regions in which the pupil images do overlap to form interferograms, the data quality is not degraded by this misalignment.

A more serious alignment problem is incorrect rotation shear. The choice of a 180-degree rotation shear (not to be confused with the 180° phase difference between Interferograms 1 and 2, attributed to conservation of energy) is central to the QPI operation. This 180-degree shear ensures that corresponding points in the upper and

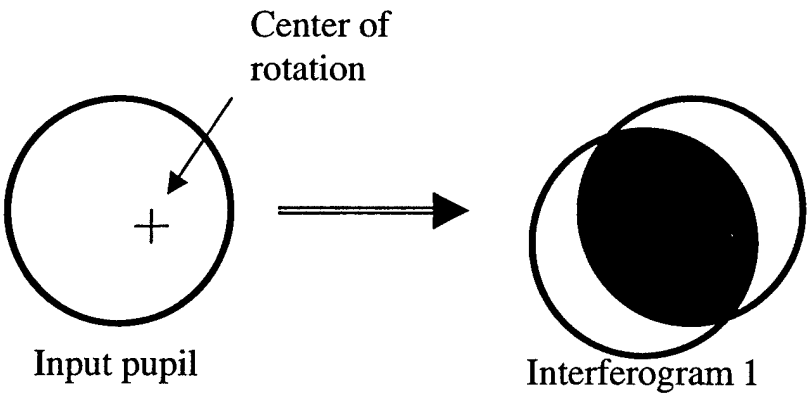

Fig. 6. Schematic representation of pupil misalignment. Misalignment of the center of the input pupil with respect to the center of rotation defined by the QPI results in imperfect overlap of the pupil images in the interferogram. Data inside the shaded region is unaffected, but the coverage of large angular frequencies is reduced.

lower quadrants are correlated. The tolerance for rotation shears different from 180 degrees depends on the spatial wavenumbers of the turbulent aberrations present. If the spatial wavenumbers are low, the tolerance is large. If the spatial wavenumbers are high, as is the case with data taken at the Hale 200″ Telescope, the tolerance is strict, on the order of 0.5 degrees.

Analysis of the data acquired at Palomar Observatory is in progress. The simplest interferograms to analyze are of Vega, a bright, pointlike source. The angular size of Vega is much smaller than the diffraction limit of the 200″ telescope at optical wavelengths (700 nm). This produces interferograms with a visibility modulus of unity everywhere. The measured visibility phase contains the phase aberrations due to the turbulence in the observing path, as well as the instrumental phase terms. A sample interferogram is shown in Fig. 8.

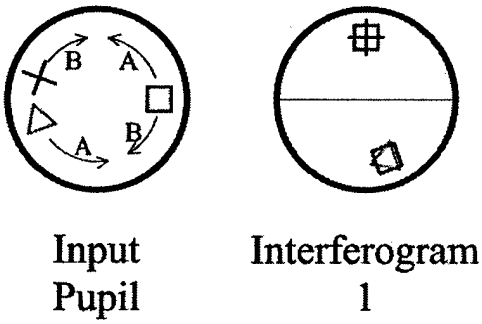

Fig. 7. Schematic representation of effect of rotation shear error. Arm A rotates its pupil image by +90 degrees, while B rotates its pupil image by -70 degrees. The net rotation shear is 160 degrees, instead of 180 degrees. The result is that the pairs of points being interfered are not duplicated in the top and bottom halves of the interferograms. If the visibility phases of these points (the triangle and cross, in this image) are sufficiently different, there is no quadrature phase relationship between these points.

The pupil position misalignment mentioned previously, due to inaccurate compensation for telescope flexure, can be readily seen in Fig. 8. The Hale 200″ Telescope is a Cassegrain system, with a small secondary mirror suspended over the primary mirror. The prime focus cage, which holds the secondary mirror, obscures the central region of the primary mirror. The result of the imperfect pupil image overlap is that the interferogram coverage is reduced near the central obscuration and near the edges of the pupil. This yields an interferogram with uneven edges and an oversized central obscuration, as shown in Fig. 8.

Because of the difficulties with real-time alignment of the interferometer, a secondary technique was used to determine the instrumental phase offset at each point in the upper quadrant than was used in the controlled laboratory experiments undertaken in the second year of effort. The most reliable way to determine the instrumental phase offset in the presence of high-wavenumber turbulent phase aberrations, without any reference to calibration data, is to examine the pixel-by-pixel covariance of intensity in the upper and lower halves of the renormalized difference, over many exposures. Assuming that the turbulent contributions to the visibility phase are uniformly distributed from zero to 2π,

$$\left\langle \cos(\phi_{\text{obj}} + \phi_{\text{turb}}) \cos(\phi_{\text{obj}} + \phi_{\text{turb}} + \theta) \right\rangle = \cos(\theta)/2,$$

where brackets denote the expectation value. This covariance is evaluated at each pixel in the upper quadrant, averaging over many exposures.

One of the significant advantages of this system is that the calibration of the instrumental phase offsets can be done using the same data that is collected for image reconstruction. A map of the covariance of the upper and lower quadrants is shown in Fig. 9. The strong covariance, and its smooth variation with position, shows that the quadrature phase offset can be obtained directly from the data itself. The exposures used to compute the covariance shown in Fig. 5 span less than one second, so this self-calibration exercise

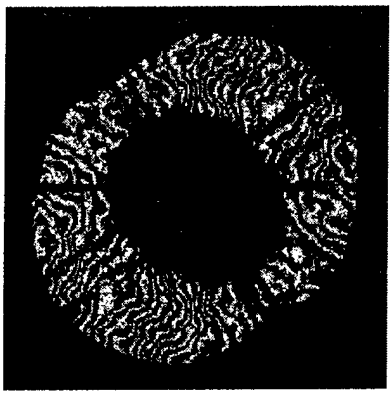

Fig. 8. Sample interferogram of Vega. This is a 12.5 ms exposure, through a 40 nm-wide bandpass filter centered at 700 nm. The visibility modulus, equivalent to the amplitude of intensity variations, is uniformly high across the interferogram. The thin horizontal gap through the center of the interferogram is the separation between upper and lower quadrants of the interferogram. The measured visibility phase due to the instrument is different in the upper and lower quadrants of the interferogram, allowing the quadrature-phase measurement.

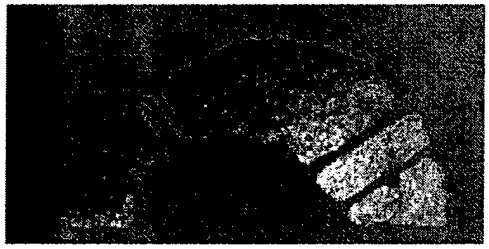

Fig. 9. Covariance of upper and lower quadrants of interferograms. The covariance of the upper and lower quadrants directly measures the cosine of the phase difference between upper and lower quadrants. The covariance shown here was calculated from 32 consecutive exposures, over a span of 0.8 s. The smooth trend and large signals allow a determination of the quadrature phase offsets without acquiring separate calibration data. Only locations in the upper quadrant are shown, which represent the covariance of corresponding (diametrically opposed) points in the upper and lower quadrants. The variation in the covariance across the upper quadrant implies that the instrumental phase offset varies smoothly with position.

could be repeated more than once per second, much faster than any variations would be expected to occur in the instrument. The measurement of this covariance, shown in Fig. 9, is the most significant result to come out of the Palomar data to date.

The measured visibility modulus, shown in Fig. 10, agrees well with the expected visibility modulus of a pointlike source. Because the angular diameter of Vega is far smaller than the diffraction-limited resolution of the Hale 200″ Telescope at visible wavelengths, the visibility modulus should be uniformly high at all angular frequencies measured. This is clearly seen in Fig. 10.

Visibility phase reconstruction is in progress, using the quadrature phase offset determined from the covariance. This test will determine the validity of the phase reconstruction technique, described in Kern et al. (2001), which relies on performing a circular average of phase gradients. The circular average requires averaging the cosine and sine components of the phase gradients separately. This technique makes use of the oversampling of the interferograms. Because the pixel scale is smaller than the turbulent coherence length, the phase difference between neighboring pixels is small. The turbulent phase differences between neighboring pixels will average to zero, leaving only the differences of the visibility phase. This reconstruction is necessary to perform

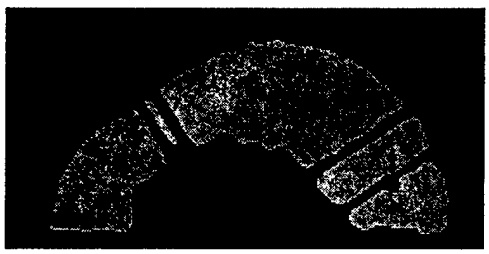

Fig. 10. Measured visibility modulus of Vega. Vega has an angular diameter far smaller than the diffraction-limited resolution of the Hale 200″ Telescope, so the visibility modulus should be uniform across the upper quadrant. The measured visibility modulus agrees well with this expectation.

accurate image reconstruction in the presence of high-wavenumber turbulent aberrations.

QPI Preparations

Preparations are under way to conduct a series of ground-to-ground imaging field tests. For these tests, a telescope with a moderate aperture (16 inches) will be attached to the QPI + KFS. A transmitting station will be sent some distance (hundreds to thousands of meters) from the QPI, where it will illuminate a test object, directing the light to the QPI. The distance between the transmitting station and the QPI can be varied, so that tests can be performed under a wide range of realistic observing conditions. Preparation for these field tests began during the period of effort for this grant, and are continuing under a new 1-year grant from AFOSR.

KFS Development

The KFS camera system has been constructed, tested, and operated under normal observing conditions. The design of the system is flexible enough to control many different parameters (voltages, time intervals), and retain a separate list of parameter settings for each readout configuration (speed, binning pattern). This allows the system to be optimized for minimum read noise in each operating configuration.

As described in Kern et al. (2001), the KFS electronics comprise a control PC, a VXI bus subsystem, and camera head electronics. The VXI bus holds a board that supplies power to the camera head electronics, a board that provides high-speed timing signals to the camera head electronics, and eight boards that each contains four high-speed Analog-to-Digital Converters (ADCs). This configuration is shown schematically in Fig. 11. The camera head electronics take power and high-speed timing signals from boards in the VXI bus, convert the timing signals into analog voltages that drive the KFS CCD, and amplify the 32 analog outputs of the CCD. These 32 analog outputs are delivered to the ADCs. The use of 32 parallel outputs on the CCD, each with an independent ADC, is critical to achieve low-noise readout with short read times.

The KFS camera system has undergone two upgrades since its inception. The first upgrade replaced the VXI enclosure, allowing an improved isolation of the analog power supplies. The second upgrade installed a liquid nitrogen cooling system, allowing the CCD to operate at low temperatures, which reduces noise due to dark current in the CCD. Each of these two upgrades resulted in an improvement in the read noise of the camera. This performance is shown graphically in Fig. 12.

The KFS camera system has been configured for full frame read times as short as 3 ms (1/333 s), and should be capable of read times down to 1.25 ms (the name Kilo-Frame per Second may prove to be a slight exaggeration). The rms read noise per pixel has been measured at 25.8 e^- for a 5 ms read time, 19.7 e^- for a 10 ms read time, and 16.3 e^- for a 20 ms read time. Pixels are often binned into 2 × 2 pixel bins, which improves the read noise for a given read time. Binned performance figures are 21.2 e^- rms for a 4 ms read time, 18.6 e^- rms for a 5 ms read time, and 15.5 e^- rms for a 10 ms read time. There are

no commercially available imaging systems that offer the pixel format, readout rate and read noise performance of the KFS system.

The camera head has also been redesigned, to reduce the risk of contamination of the CCD and to make the connectors more convenient to attach and detach. The number of connectors will be reduced to 4, from 34. The shutter will be located outside of the camera head, reducing the transfer of dust particles onto the CCD. The components of the new camera head have been fabricated but not yet assembled and mated to the KFS CCD.

HIT-KFS CCD Development

The HIT-KFS CCD began development under this program. The low-noise operation of the KFS CCD at high speeds is enabled by the 32 independent analog output channels on the CCD, which reduce the analog bandwidth (and corresponding noise) at each output relative to a single-output system. The HIT-KFS CCD greatly expands this advantage, by utilizing 256 independent analog output channels. This large number of channels is multiplexed down to 32 analog signals to be digitized, utilizing low-noise, low-cost CMOS technology located on-chip. CMOS circuits are bump-bonded to the silicon CCD, enabling the use of these complementary technologies to their mutual advantage.

The reduced bandwidth at each CCD output amplifier results in a significant

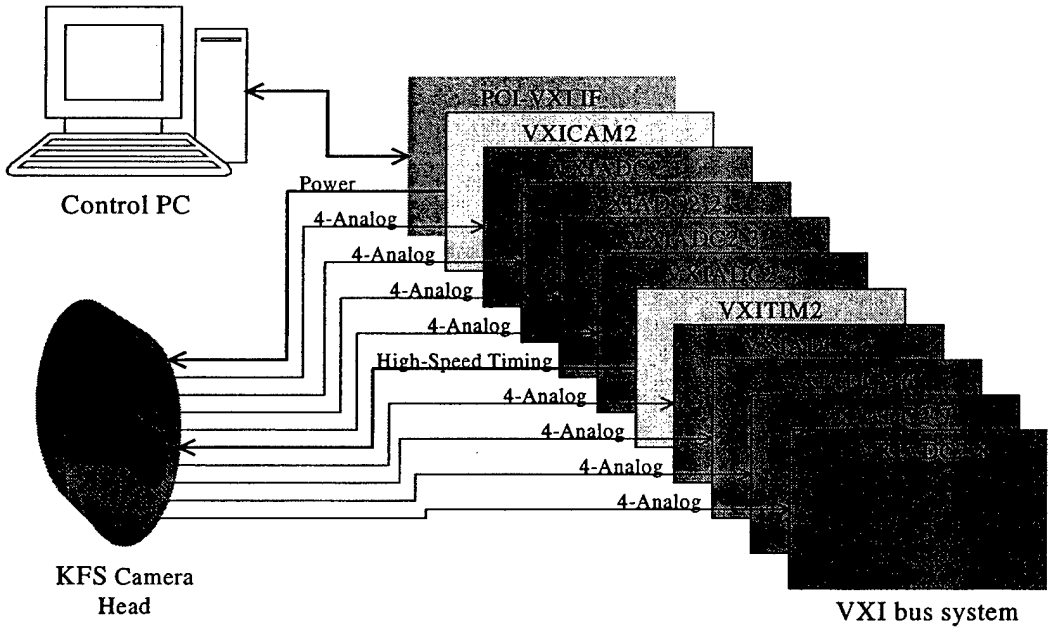

Fig. 11. Schematic representation of KFS camera system electronics. A control PC communicates with a VXI bus subsystem, which controls the KFS camera head electronics. Each board in the VXI bus subsystem is shown, including the eight boards with 4 ADC channels each.

improvement in expected noise performance. The expected rms read noise is <3 e^-/pixel, with a 33 ms read time, and under 10 e^-/pixel with a 5 ms read time. Because the light-sensitive components are nearly identical to the currently existing KFS system, this improvement in read noise performance comes with no degradation to the sensitivity or format (1024 × 1024 pixels) of the system.

The design and fabrication of the CCD and CMOS components has been completed, and packaging, delivery, and testing of the devices will occur during the period of effort of a subsequent AFOSR grant.

Conclusions

The experiments undertaken during the period of effort have demonstrated the fundamental principles of quadrature phase interferometry, including imaging in the presence of weak turbulent aberrations, obtaining self-calibration phase data, and measuring the visibility modulus of simple objects under ordinary observing conditions. The KFS camera system has been optimized for low read noise at high frame rates. The QPI + KFS system will undergo a series of field tests under realistic observing conditions, during the period of effort of a recently activated 1-year AFOSR grant.

The research conducted under this program was partially funded by NSF Grant AST9618811, and continues under AFOSR Grant F49620-03-1-0102.

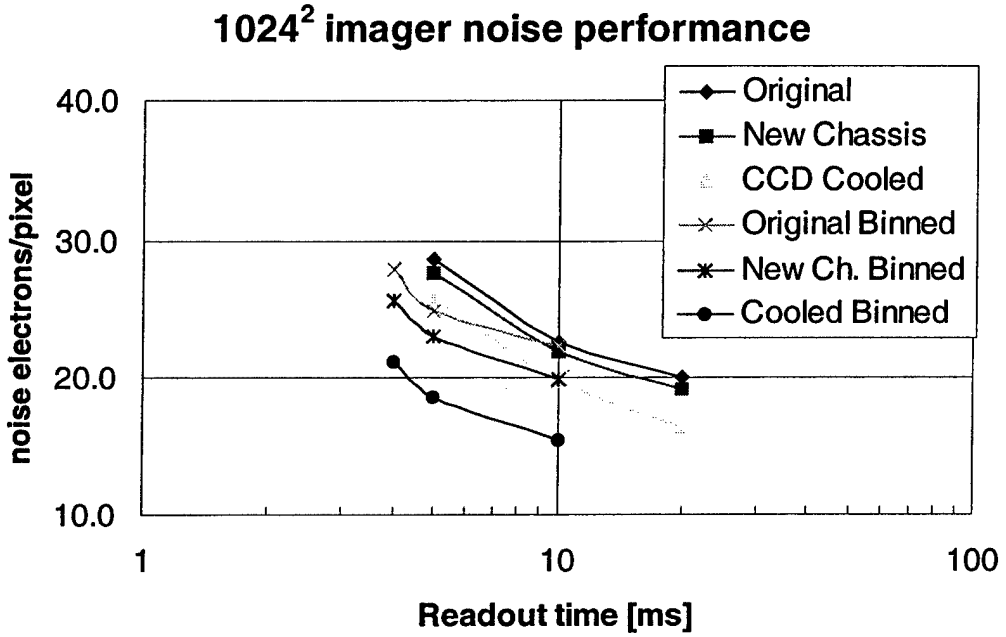

Fig. 12. KFS read noise versus read time. The performance of the KFS camera system is shown for several different configurations. The most current configurations are the cooled configurations, in either full-frame (CCD Cooled) or (2×2)-pixel binned mode (Cooled Binned).

References Cited

Fried, D.L. 1966, "Optical Resolution Through a Randomly Inhomogeneous Medium for Very Long and Very Short Exposures," *Applied Optics* **56**, 1372-1379.

Kern, B., Lang, D.B., Martin, C., Dimotakis, P.E., Wadsworth, M. 2001, "A High-Speed Quadrature-Phase Rotation-Shearing Interferometer for Imaging Through Turbulence," *32nd AIAA Plasmadynamics and Lasers Conference*, AIAA 2001-2797.

Research Personnel Supported

- Dimotakis, P.E., John K. Northrop Professor of Aeronautics and Professor of Applied Physics (PI)
- Katzenstein, G., Research Engineer, Aeronautics (since September 2001)
- Kaye, S., Electrical Engineer, Physics
- Kern, B., Graduate Student, Astronomy (until June 2002), Postdoctoral Fellow, Aeronautics (after June 2002)
- Lang, D.B., Research Engineer, Aeronautics
- Martin, C., Professor of Physics (Co-I)
- Mojahedi, C., Administrative Assistant, Aeronautics (since October 2001)
- Svitek, P., Research Engineer, Aeronautics (until 2000)
- Thessin, R., Undergraduate Student, Applied Physics (since June 2002)

Collaborators

- Atlas, G., President and CEO, Imager Labs (HIT design)
- Boyadzhyan, V., Research Engineer, Jet Propulsion Laboratory (KFS, HIT design / fab)
- Bredthauer, R., Research Engineer, Jet Propulsion Laboratory (KFS fab)
- Collins, S.A., Research Engineer, Jet Propulsion Laboratory (KFS, HIT design / fab)
- Dingizian, A., Research Engineer, Jet Propulsion Laboratory (KFS, HIT design / fab)
- Elliott, S.T., Research Engineer, Jet Propulsion Laboratory (KFS, HIT design / fab)
- Kullman, R., Vice-President and Business Manager, Imager Labs (HIT design)
- Wadsworth, M.W., Research Engineer, Jet Propulsion Laboratory (KFS, HIT design / fab)

- Palomar Adaptive Optics Group, meetings with R. Dekany, T. Tombrello, V. Velur, M. Fischer

Honors / Awards

Honors, degrees, and awards received during period, as well as, "lifetime achievement honors such as Nobel prize, honorary doctorates, and society fellowships prior to this effort":

- Dimotakis, P.E.:

  John K. Northrop Chair, Aeronautics, Caltech (February 1995)

  Associate Fellow, AIAA (June 1989)

  Fellow, Am. Phys. Society (November 1980)

- Martin, C.:

  Uhl Prize for Outstanding Research in Astrophysics, U.C. Berkeley (1985)

- Kern, B.:

  Ph.D., California Institute of Technology (June 2002)

  Michelson Postdoctoral Fellowship Award (July 2002)

Publications of work supported under this Grant

Kern, B., Laurence, T.A., Martin, C., Dimotakis, P.E. 2000, "Temporal coherence of individual turbulent patterns in atmospheric seeing," *Applied Optics* **39**, 4879-4885.

Kern, B., Lang, D.B., Martin, C., Dimotakis, P.E., Wadsworth, M. 2001, "A High-Speed Quadrature-Phase Rotation-Shearing Interferometer for Imaging Through Turbulence," *32nd AIAA Plasmadynamics and Lasers Conference*, AIAA 2001-2797.

Dimotakis, P.E., Catrakis, H.J., Fourguette, D.C. 2001, "Flow structure and optical beam propagation in high-Reynolds-number gas-phase shear layers and jets," *Journal of Fluid Mechanics* **433**, 105-134.

Kern, B., Martin, C. 2002, "Optical pulsations from the anomalous X-ray pulsar 4U0142+61," *Nature* **417**, 527-529. (The research in this paper, while not a direct product of the AFOSR grant reported here, made use of dual-purpose equipment shared with the QPI, purchased with this AFOSR grant.)